Volume 1 | Number 1 | Jan 2013 | Pages 1–100

PCCP

Physical Chemistry Chemical Physics
www.rsc.org/pccp

ROYAL SOCIETY OF CHEMISTRY

ROYAL SOCIETY OF CHEMISTRY

www.rsc.org/pccp

Journal Name

ARTICLE

Morphology, Molecule Stacking, Dynamics and Device Performance Correlations in Vacuum-Deposited Small-Molecule Organic Solar Cells

Chang-Wen Chen,[a] Zheng-Yu Huang,[a] Yi-Min Lin,[a] Wei-Ching Huang,[a] Yi-Hong Chen,[a] Joseph Strzalka,[b] Angela Y. Chang,[c] Richard D. Schaller,[c,d] Cheng-Kuang Lee,[e] Chun-Wei Pao[e] and Hao-Wu Lin[*][a]

The "all carbon" organic solar cells (OSCs) based on the homocyclic molecule Tetraphenyldibenzoperiflanthene (DBP) as a donor and C60 as an acceptor were comprehensively characterized. The optimized planar-mixed heterojunction device with a DBP:C60 mixture ratio of DBP:C60 (1:2) exhibited a power conversion efficiency of 4.47%. To understand why DBP possesses such advantageous characteristics, the correlations of the morphology, molecule stacking, carrier dynamics and performance of DBP:fullerene-based devices have been systematically studied. First, the face-on stacked DBP molecules could enhance both the absorption of light and the charge carrier mobility. Second, DBP:C60 (1:2) thin films with optimized domain sizes and partially interconnected acceptor grains led to the most balanced carrier mobility and the lowest bi-molecular recombination in devices. Final, the DBP molecules were found to stack closely using grazing incidence wide-angle X-ray scattering measurement, with a π-π stacking spacing of 4.58 Å, indicating an effective molecular orbital overlap in DBP. The study not only reveals the promising characteristics of DBP as donors in OSCs but the clear correlations of the thin-film nano-morphology, molecular stacking, carrier mobility and charge recombination found here could also provide insights into the characterization methodology and optimization for the small molecule OSCs.

Introduction

Organic solar cells (OSCs) are a promising candidate for solar energy-harvesting devices, which have been investigated intensively due to their advantages of low-cost, low energy consumption in fabrication, short energy payback time and mechanical flexibility.[1-9] Among these devices, vacuum-deposited small-molecule organic solar cells (SMOSCs) exhibit the predominant advantages of well-defined molecular structures, high-quality purification by thermal gradient sublimation, amenability to large-scale production, better batch-to-batch reproducibility and ready adoption into the successful organic light emission display (OLED) industry; these advantages have been significantly improved recently, due to the incorporation of new donor materials, the sophistication of device structures and improved control of the active-layer morphology.[10-16] To date, power conversion efficiencies (PCEs) of up to 5~7% have been reported in vacuum-deposited SMOSCs using symmetrical heterocyclic,[17-24] asymmetrical heterocyclic[25-29] and homocyclic donors.[30-36] The later one is

the most intriguing class of materials because when they are paired with fullerene C60 or C70 acceptors, the only element, except for hydrogen, in the active layer is carbon. Consequently, a true "all-carbon" photovoltaic device can be realized. Tetraphenyldibenzoperiflanthene (DBP) is one of the homocyclic donors that has been used in a SMOSC device to demonstrate the highest efficiency so far.[37, 38] To understand why DBP possesses such advantageous characteristics, comprehensive ellipsometric analysis, temperature dependent carrier mobility measurements, application of transient photovoltage and photocurrent techniques, femtosecond transient absorption spectroscopy, impedance spectroscopy, grazing incidence wide-angle X-ray scattering (GIWAXS) and recombination kinetic modelling are used to investigate the correlations of the morphology, molecule stacking, carrier dynamics and performance of DBP:fullerene-based devices. The nanoscale morphology, degree of crystallinity and molecular packing in the thin films were studied using GIWAXS. Spectroscopic ellipsometry was used to identify the statistically averaged molecular orientation of DBP in both
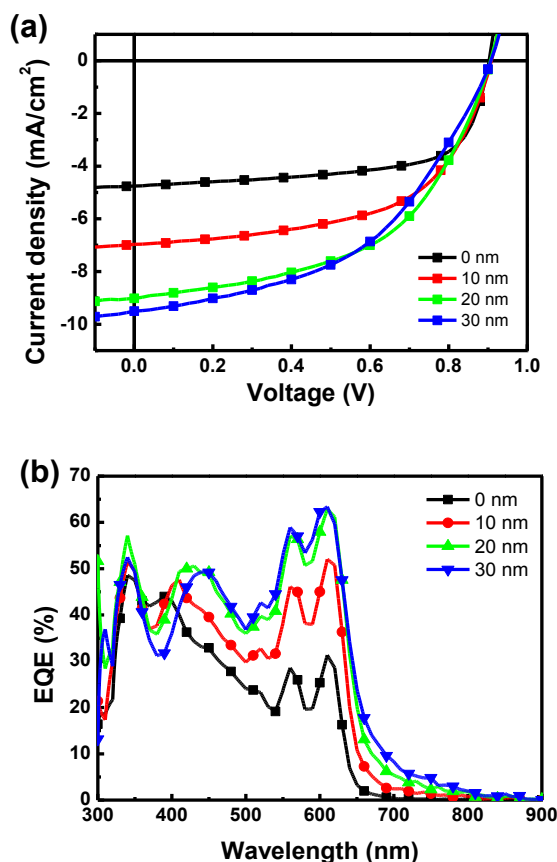
Figure 1. (a) J-V characteristics (under 1 sun, AM 1.5G illumination) and (b) EQE spectra of PMHJ devices with the mix layer thickness of 0 nm (squares), 10 nm (circles), 20 nm (triangles) and 30 nm (inverted triangles).

Table 1. Performance parameters of the DBP:C60 (1:1) PMHJ devices with different thicknesses of the mixed layer and the optimized PHJ devices.

Thickness of the mixed layer	J_{sc} (mA cm^{-2})	V_{oc} (V)	FF (%)	PCE (%)
0 nm	4.75	0.903	0.66	0.66
10 nm	6.98	0.910	0.57	3.63
20 nm	9.02	0.906	0.52	4.26
30 nm	9.11	0.906	0.48	4.07

DBP neat films and DBP:fullerene blend films. Moreover, transient photovoltage and photocurrent techniques, femtosecond transient absorption spectroscopy, impedance spectroscopy, as well as temperature-dependent space-charge-limited-current (SCLC) mobility measurement revealed the carrier dynamics in the DBP:fullerene mixtures, such as the carrier lifetime, charge transportation and recombination. The carrier mobility and recombination mechanisms were found to be highly related to the DBP:fullerene nanostructures, which were controlled by the DBP:fullerene composition ratio. Retarded charge recombination, balanced electron and hole mobilities, as well as effortless carrier transportation in an

optimized nano-scale morphology all contributed to the high PCE of the fine-tuned DBP:C_{60} devices.

Results and Discussions

Device characterization

The vacuum-deposited planar-mix heterojunction (PMHJ) devices based on DBP as a donor and C_{60} as an acceptor were fabricated. The active layers of the PMHJ device were composed of a DBP:C_{60} mixture layer sandwiched between a homogeneous donor and acceptor layer, which provides efficient photon harvesting and exciton dissociation due to the larger donor/acceptor (D/A) interfacial area. The devices were configured as glass/ITO/PEDOT:PSS/MoO$_3$ (5 nm)/DBP (10 nm)/DBP:C_{60}/C_{60} (20 nm)/Bphen (6 nm)/Ag (100 nm). The MoO$_3$ thin film acted as the hole extraction layer, and the Bphen thin film served as the electron extraction layer. First, the thicknesses of DBP:C_{60} (1:1) mixture layers were tuned to optimize the device performance. Figure 1(a) shows the current density to voltage (*J*-V) characteristics for devices under simulated AM 1.5G solar illumination (100 mW/cm^2), and the device performance parameters are summarized in Table 1. The short-circuit current density (J_{sc}) increases with
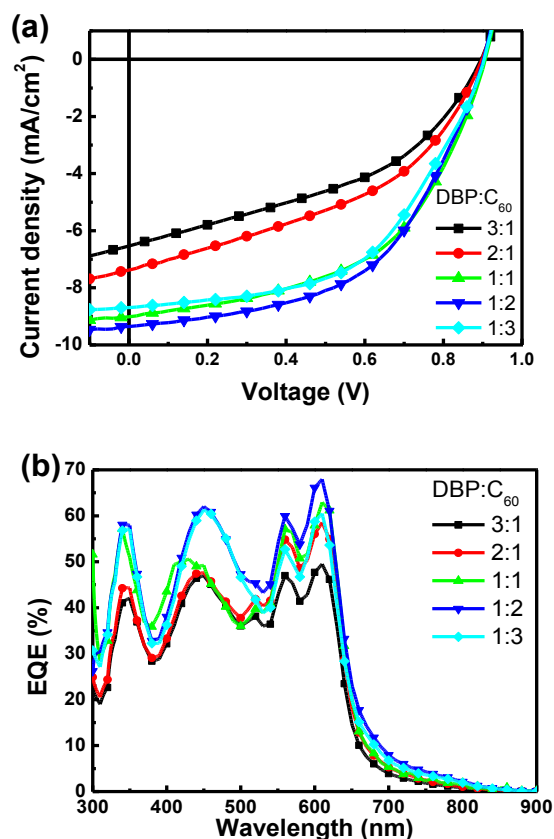

Figure 2. (a) J-V characteristics (under 1 sun, AM 1.5G illumination) and (b) EQE spectra of DBP:C60 PMHJ solar cells with the volume ratio of 3:1 (squares), 2:1 (circles), 1:1 (triangles), 1:2 (inverted triangles) and 1:3 (diamonds).

Table 2. Performance parameters of the DBP:C60 PMHJ devices with different D/A ratios of the mixed layer.

Thickness of the mixed layer	J_{sc} (mA cm^{-2})	V_{oc} (V)	FF (%)	PCE (%)
3:1	4.75	0.903	0.66	0.66
2:1	6.98	0.910	0.57	3.63
1:1	9.02	0.906	0.52	4.26
1:2	9.11	0.906	0.48	4.07

the thickness of the active DBP:C$_{60}$ layer due to the increase of the optical absorption. However, the fill factor (FF) decreases with the increase of the active layer thickness because of the reduction in the charge collection efficiency. The optimized device with a 20-nm DBP:C$_{60}$ layer resulted in a J_{sc} of 9.02 mA/cm^2, a V_{oc} of 0.906 V and a FF of 52.2%, leading to a PCE of 4.26%. The external quantum efficiency (EQE) spectra of the cells are shown in Figure 1(b).

To further optimize the device efficiency, we then fixed the thickness of the DBP:C$_{60}$ layer to 20 nm and investigated the performance of the devices with various DBP:C$_{60}$ blend ratios. The J-V characteristics and the EQE spectra of the DBP:C$_{60}$ (3:1, 2:1, 1:1, 1:2 and 1:3) devices are shown in Figure 2(a) and 2(b), respectively. The performance of the devices is also summarized in Table 2. The best performance was obtained in the DBP:C$_{60}$ (1:2) device. Interestingly, devices with DBP-rich mixture layers exhibited lower J_{sc} and FF compared to the devices with the C$_{60}$-rich mixture layers. From the EQE results, the DBP-rich devices exhibited a lower EQE across entire the wavelength range, indicating that the DBP-rich mixture layers likely possess a low D/A interfacial area or/and discontinuous domain structure, leading to the higher charge carrier or exciton recombination and unbalanced carrier mobilities. The mechanisms were further investigated using AFM, SCLC, ac impedance, TPV and TPC measurements. (*vise infra*).

Optical characteristics

Detailed optical properties provide information on the molecular stacking, which plays a significant role in the performance of the devices.[39, 40] Thus, we analysed the optical properties of the active layers to clarify the relationship between the DBP:C$_{60}$ blend ratio and the donor molecular stacking. Variable-angle spectroscopic ellipsometry (VASE) was utilized to investigate the anisotropic optical properties of a DBP neat film and DBP:C$_{60}$ with different blend ratios. To extract the relatively complicated in-plane and out-of-plane optical constants, VASE measurement in transmission and reflection mode must be performed.[41] Kramers-Kronig consistent models with a combination of Gaussian oscillators (~ 8 for in-plane and ~ 5 for out-of-plane) were constructed to model the in-plane and out-of-plane optical constants of the films. Figure 3 shows the extracted refractive index (n) and extinction coefficient (k) in the horizontal direction (in-plane, n_o, k_o) and the perpendicular direction (out-of-plane, n_e, k_e) of the DBP neat film, respectively. n_o and k_o are both much higher than n_e and k_e, i.e., a significant optical anisotropy was observed, which indicates that the molecular plane is oriented in the horizontal direction.[41, 42] However, the horizontal orientation of the DBP molecules may not be retained in vacuum-deposited DBP:C$_{60}$ mixture films. To investigate the properties of the DBP:C$_{60}$ blends, the ellipsometric data of DBP:C$_{60}$ blended thin films with different ratios of DBP:C$_{60}$ were also measured, with the

extracted optical constants shown in Figure 4. The higher k_o value than the k_e value at the absorption peaks of DBP can still be observed in the DBP:C$_{60}$ mixture films. As the concentration of C$_{60}$ increases, the difference between n_o and n_e as well as between k_o and k_e drops due to the dilution effect of the C$_{60}$. However, detailed analysis of the k_o/k_e of DBP:C$_{60}$ with various composition ratios (including DBP neat film) at the DBP absorption peak (~ 605 nm) reveals a comparable value in all of the samples, which indicates that the horizontal orientation of the DBP molecules in DBP:C$_{60}$ blend is similar to that in the DBP neat film, regardless of the DBP:C$_{60}$ ratio. The horizontal stacking of the DBP and the higher k_o may contribute to the higher light absorption and improved hole transport. However, because DBP exhibits a similar orientation tendency in the films with different DBP:C$_{60}$ ratios, the orientation of the DBP molecules may not be the main factor in the DBP:C$_{60}$ ratio-dependent device performance.
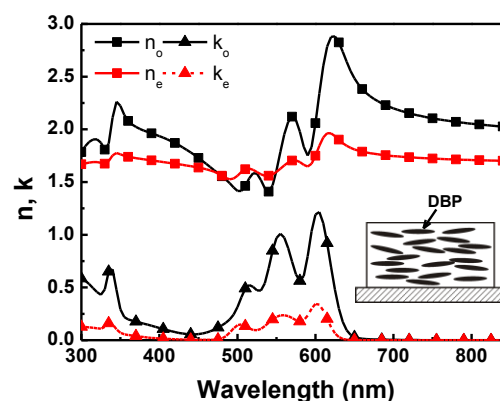

Figure 3. Optical constants of a DBP thin film. The black line with squares and triangles represents the in-plane (horizontal) and out-of-plane (perpendicular) refractive index (n_o and n_e), respectively, and the red line with squares and triangles represents the in-plane (horizontal) and out-of-plane (perpendicular) extinction coefficient (k_o and k_e), respectively.

Surface morphology

In OSCs, the surface morphology of the active layer may reveal some useful information regarding the performance of the devices.[25, 43-47] A large D/A interfacial area with bicontinuous charge carrier pathways is essential for effective exciton dissociation and charge carrier transport. Thus, we analysed the surface nano-scale morphology of the DBP:C$_{60}$ mixture films with various ratios (3:1, 1:1 and 1:2) by tapping mode atomic force microscopy (AFM), and the phase images are shown in Figure 5. Surface topography images of the thin films exhibited similar smooth morphologies with a root mean square roughness of 0.25 nm in all blend ratios, but the phase images revealed distinct phase-separated formations. In the DBP:C$_{60}$ (3:1) blend film, the acceptor grains dispersed in the donor matrix, leading to a small D/A interfacial area and discontinuous pathways for electron transport. With the short exciton diffusion length of organic semiconductors, the average distance between the acceptor grains is too long for excitons to successfully arrive at the D/A interface, leading to a low J_{sc} in the DBP:C$_{60}$ (3:1) device. Discontinuous acceptor pathways result in the unbalanced charge carrier mobilities in the mixed layer, which is expected to cause the reduction of the FF in the DBP:C$_{60}$ (3:1) cell. However, DBP:C$_{60}$

(1:1) and DBP:C$_{60}$ (1:2) thin films both exhibited fine domain structures, which induced a large D/A interfacial area, and thus a high exciton dissociation efficiency.
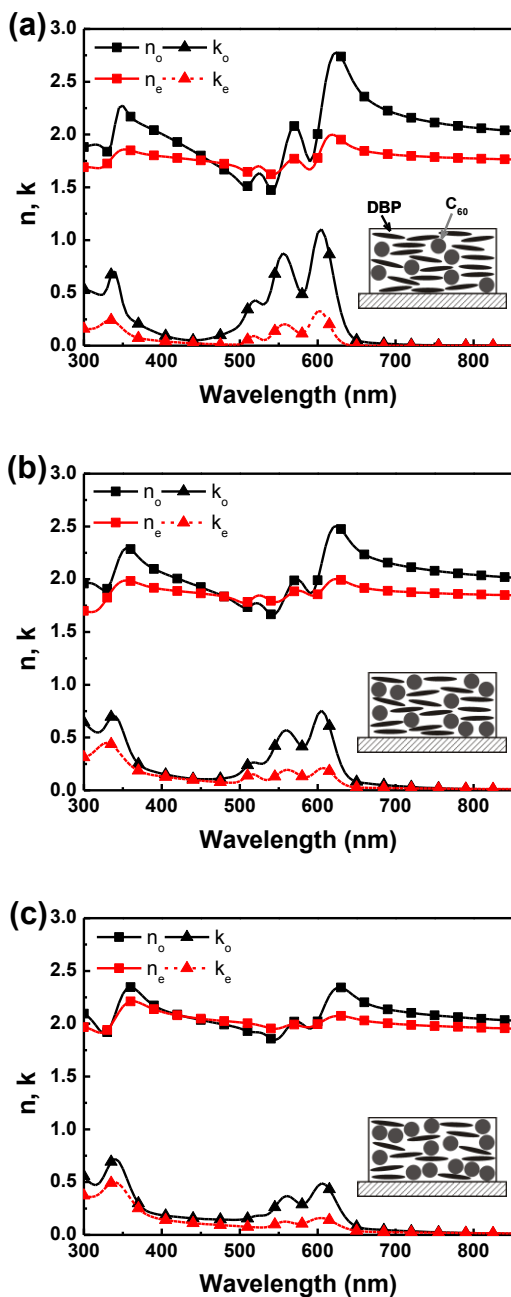

Figure 4. Optical constants of DBP:C60 blended thin films with the ratios of (a) 3:1, (b) 1:1 and (c) 1:2.

Charge carrier mobility

To examine the influence of the above-mentioned molecular stacking and thin-film morphology on the electronic properties, space charge limited current (SCLC) measurements were used to evaluate the carrier mobility in the DBP:C$_{60}$ layer with various blend ratios.[48, 49] We fabricated the hole-only and electron-only devices with the structures of: glass/ITO/MoO$_3$ (1 nm)/
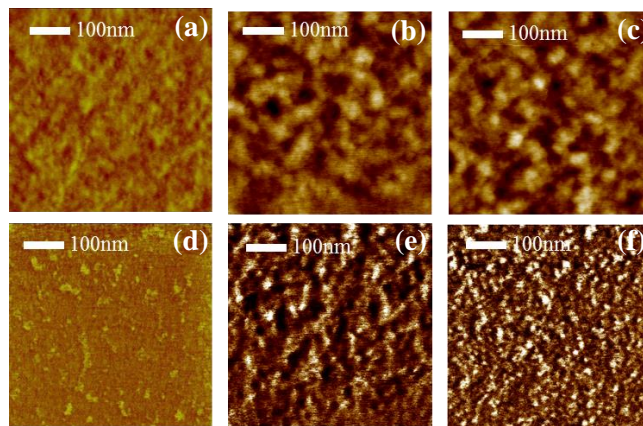

Figure 5. AFM topology (left) and phase (right) image of co-deposited (a and b) DBP:C60 (3:1), (c and d) DBP:C60 (1:1) and (e and f) DBP:C60 (1:2) blended thin films.

DBP:C$_{60}$ (100 nm)/MoO$_3$ (10 nm)/Al (150 nm) and glass/ITO/Mg (5 nm)/DBP:C$_{60}$ (100 nm)/Ca (5 nm)/Al (150 nm), respectively. The fitted carrier mobilities are shown in Figure 6. The hole and electron mobilities of the DBP:C$_{60}$ (1:2) film were 1.58×10^{-4} and 1.23×10^{-4} cm^{2}V^{-1}s^{-1} at 700 (V/cm)$^{-0.5}$, respectively, which exhibited the most balance in the mobilities among all of the blend ratios considered, thus contributing to the highest performance under solar illumination. In contrast, the hole and electron mobilities in the DBP:C$_{60}$ (3:1) mixed film were considerably unbalanced with the values of 1.22×10^{-4} and 4.81×10^{-7} cm^{2}V^{-1}s^{-1} at 700 (V/cm)$^{-0.5}$, respectively. Compared to DBP:C$_{60}$ (1:2), the DBP:C$_{60}$ (3:1) film exhibited a similar hole mobility, but exhibited a three orders-of-magnitude lower electron mobility. This result has good correlation with the surface morphology observed using AFM. The island-like acceptor grains are not able to provide a continuous pathway for electron transport, leading to a very low electron mobility and unbalanced charge carrier transport characteristics, which is further reflected in the low J_{sc} and FF of the DBP:C$_{60}$ (3:1) device.
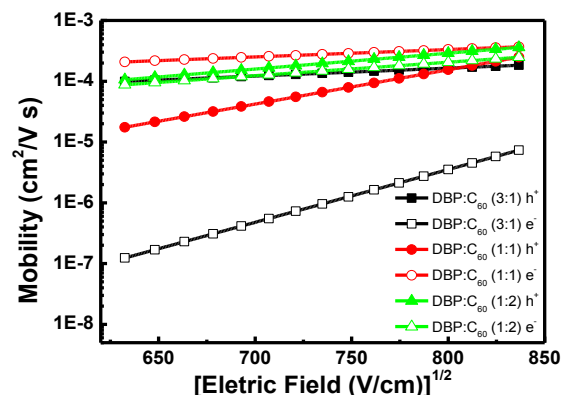

Figure 6. Hole (solid) and electron (hollow) mobilities for the DBP:C60 (3:1) (squares), DBP:C60 (1:1) (circles) and DBP:C60 (1:2) (triangles) blended thin films.

Table 3. Performance parameters of the DBP:C60 PMHJ devices with different D/A ratios of the mixed layer.

Device type	μ_p (cm^2 V^{-1} s^{-1})	σ	Σ
DBP:C60 (1:1) hole	0.0029	0.1335	1.500
DBP:C60 (1:1) electron	0.0545	0.1045	3.208
DBP:C60 (1:2) hole	0.0792	0.1363	3.351
DBP:C60 (1:2) electron	0.0373	0.1243	2.330

Energetic and positional disorder

A deeper insight into the correlation between the carrier mobility and the morphology of the DBP:C$_{60}$ layer can be obtained by analyzing the temperature-dependent SCLC data using the Gaussian disorder model.[50-52] The model is based on the concept of charge hopping. Energetic disorder (σ) and positional disorder (Σ) are used to describe the transport of carriers in random organic solids. Energetic disorder is the Gaussian width related to the random-variables energy, which comes from the distribution of the energy states. Positional disorder is the Gaussian width related to the overlap parameter, which arises from structural or chemical defect.[53] The carrier mobility can be expressed using the Bässler formalism:

$$\mu(E,T) = \mu_p \exp\left(-\left(\frac{2\sigma}{3k_BT}\right)^2\right)\exp\left(C\left(\left(\frac{\sigma}{k_BT}\right)^2 - \Sigma^2\right)\sqrt{E}\right), \qquad (1)$$

where E is the applied electric field, T is the absolute temperature, k_B is the Boltzmann constant, μ_p is the prefactor mobility and C is the empirical constant. This equation can be used to analyse the temperature-dependent carrier mobility and extract the σ and Σ parameters of the blend films. Figures S1 and S2 show both the temperature-dependent hole and electron mobilities for the DBP:C$_{60}$ (1:1) and (1:2) thin films, respectively. A good match between the experimental and the modelled data is found. The extracted parameters are listed in Table 3. In DBP:C$_{60}$ (1:1) and (1:2) thin-films, the hole σ values were nearly identical. However, the DBP:C$_{60}$ (1:1) film exhibited a lower electron σ value than that in the DBP:C$_{60}$ (1:2) film. This lower value may due to the equal mole ratio in the DBP:C$_{60}$ (1:1) film. Furthermore, the DBP:C$_{60}$ (1:1) film exhibited a lower hole Σ value but a higher electron Σ value compared to the DBP:C$_{60}$ (1:2) layer, indicating that the distance between each DBP molecule became varied, while C$_{60}$ was more equally distributed as the C$_{60}$ concentration increased. The above-mentioned blend morphology is schematically illustrated in Figure 7.

AC impedance measurement

While the SCLC measurement revealed the electronic characteristics of the DBP:C$_{60}$ blend film, the electronic properties of the complete DBP:C$_{60}$ devices were further studied using alternating current (AC) impedance spectroscopy. AC impedance spectroscopy is a powerful tool for the investigation of the interface and bulk
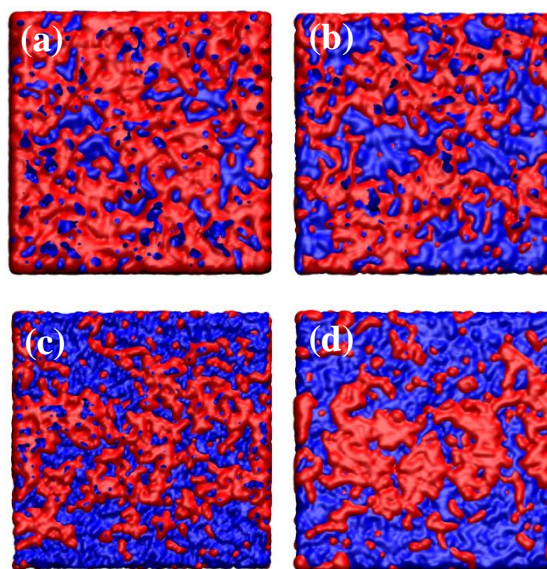

Figure 7. Illustrations of the DBP:C60 morphologies with ratios of (a) 3:1, (b) 1:1, (c) 1:2 and (d) 1:3.

electronic properties and the charge carrier characteristics of optoelectronic devices.[54-56] Due to the different speeds of the electrical response of each component in the device, the electrical properties of the bulk and the interface could be analysed by monitoring the current response as a function of the applied voltage frequency. This method has been intensively used to analyse the charge carrier relaxation and transport in dye-sensitized solar cells[57-59] and organic light emitting diodes.[60-62] In recent years, the method has also been used to characterize the electrical properties of OSCs.[63-67]
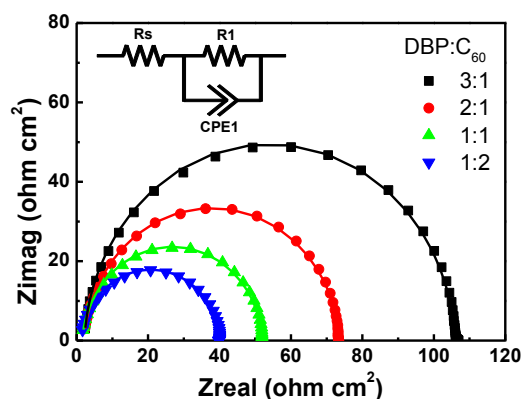

Figure 8. The Nyquist plots (symbols) obtained from the DBP:C60 PMHJ cells operated in the dark and near the Voc condition and the fitting curves (solid lines) calculated according to the equivalent circuit model (inset).

The impedance spectra of the DBP:C$_{60}$ OSCs were measured under simulated 1-sun illumination and in the dark. The illuminated devices were operated in V$_{oc}$ condition, and the devices in the dark were biased with an additional voltage of 0.9 V. Figure 8 depicts the Nyquist plots of the DBP:C$_{60}$ (3:1, 2:1, 1:1 and 1:2) devices operated in the dark. We observed that the curves were fairly close to a

semicircle and can be modelled with the equivalent circuit shown in the inset of Figure 8. The equivalent circuit consists of a series connection of a series resistance (R_s) and a parallel resistance-constant phase element circuit ($R_I \| CPE_1$). $R_I \| CPE_1$ represents the depressed semicircles observed in the Nyquist plots. The extracted parameters are listed in Table 4. As shown in Figure S3 and Table S1, the AC characteristics of the devices under 1-sun illumination follow the same trend as the case of operation in the dark. The largest R_I value of the DBP:C_{60} (3:1) device indicates that charge carriers are blocked, which resulted in the lowest FF in these devices. In contrast, the lowest R_I value of the DBP:C_{60} (1:2) device represents good charge carrier transport in the active layer, and thus the device exhibited the highest FF and PCE. The R_I value and the size of the semicircles decrease with the increase of the C_{60} ratio, which may be due to the increase of the electron mobility in C_{60}-rich devices, as found in the SCLC measurements.

Table 4. The parameters of the equivalent circuit for the cells in the dark near the Voc condition.

DBP:C_{60}	R_s ($\Omega\,cm^2$)	R_I ($\Omega\,cm^2$)	CPE_1 ($nF\,cm^{-2}$)
3:1	2.2	103.8	77.5
2:1	2.1	71.6	101.6
1:1	1.6	50.5	108.4
1:2	1.3	38.9	126.4

Transient photovoltage and transient photocurrent measurements

Transient photovoltage (TPV) and transient photocurrent (TPC) measurements were used to obtain the values of the carrier recombination lifetime (τ_n) and the charge density in the OSCs.[68-72] The TPV decays were used to extract τ_n through a pseudo-first-order rate equation,

$$\frac{d\Delta V}{dt} \propto \frac{d\Delta n}{dt} = \frac{\Delta n}{\tau_n}, \qquad (2)$$

where ΔV is the amplitude of the TPV, t is the time and Δn is the change in the carrier density due to the laser pulse.[68, 69] The steady-state carrier concentration at V_{oc} can be determined by

$$n = \frac{1}{Aed}\int_0^{V_{oc}} C dV, \qquad (3)$$

where C is the differential capacitance, A is the device area, e is the electronic charge and d is the thickness of active layer. C was calculated using

$$C = \frac{Q}{\Delta V}, \qquad (4)$$

where ΔV is the amplitude of the TPV. Q denotes the injected charges upon excitation, which could be measured by the TPC.

Figure 9 shows the carrier lifetime versus the carrier density of the DBP:C_{60} devices with different blend ratios. Intriguingly, the carrier density of the DBP:C_{60} (3:1) device is higher than that of the DBP:C_{60} (1:2) device, suggesting a higher J_{sc} exists
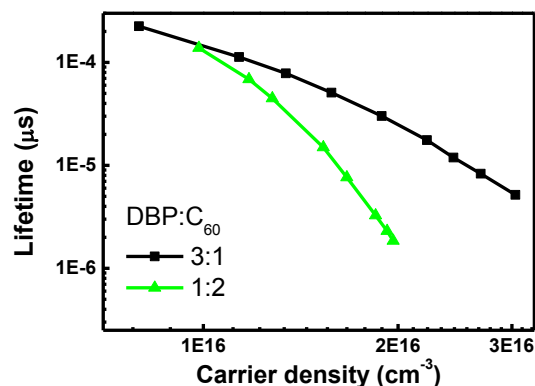

Figure 9. Carrier lifetime measured determined using the transient photovoltage versus the carrier density modified by the variable bias light intensity for DBP:C60 (3:1) (squares), DBP:C60 (1:1) (circles) and DBP:C60 (1:2) (triangles) blended thin films.

in the DBP:C_{60} (3:1) device. However, this suggestion contradicts the J_{sc} values observed in the actual devices. This discrepancy may be attributed to the different interfacial areas and the pathway morphologies of the charge carrier extraction. The higher carrier density in the device could result not only from a higher photogeneration but also from a slower exciton recombination. Because the absorption is approximately the same in films with various DBP:C_{60} ratios, the higher carrier density is more likely caused by the slower exciton recombination. For organic semiconducting mixtures, it has been shown that the bimolecular recombination process can be described by the Langevin expression, which indicates that the recombination rate is dominated by the carrier mobility of the slower charge carrier because the electrons and holes are confined to different phases in the blend.[73, 74] The lower electron mobility in the DBP:C_{60} (3:1) blend, as shown in Figure 6, could result in a slower recombination rate and thus a higher carrier density, which is not beneficial to the device performance.

Recombination kinetics

Monomolecular recombination and bimolecular recombination all contributes to efficiency loss in OSCs.[73, 75-77] To clarify the dominant recombination process in the DBP:C_{60} system, J-V curves at different incident light intensities were modelled using a simple model constructed with the drift and continuity equations. In this model, the current is divided into two parts.

$$J(V) = J_{ph}(V) + J_{dark}(V), \qquad (5)$$

where J_{ph} is the photocurrent and J_{dark} is the dark current. J_{dark} here is assumed to be a constant at different incident light intensities. J_{ph} can be calculated using the drift equation:

$$J_{ph}(V) = en(V)\mu E(V), \qquad (6)$$

where n is the charge density, μ is the mobility and E is the internal electric field which is assumed homogeneous in the active layer:

$$E = \frac{V_s - V}{d}, \tag{7}$$

where V is the applied voltage and d is the thickness of the active layer. V_s is the built-in-voltage at which the current under illumination is equal to the dark current, i.e., at which the photocurrent equals zero. Another important equation used in this model is the continuity equation:

$$\frac{J_{ph}}{e} = (G - R)d, \tag{8}$$

where G is the generation rate and R is the recombination rate, which can be further divided into the mono- and the bi-molecular recombination rates.

$$R = R_{mono} + R_{bi}, \tag{9}$$

$$R_{mono} = \frac{n}{\tau}, \tag{10}$$

$$R_{bi} = \gamma n^2, \tag{11}$$

where R_{mono} is the monomolecular recombination rate, τ is the monomolecular recombination lifetime, R_{bi} is the bimolecular recombination rate and γ is the bimolecular recombination coefficient. The monomolecular recombination here includes all types of losses, which are proportional to the charge densities. In a more precise model, there should be a coefficient in front of the generation rate to describe the losses before charge separation. However, because the influence of these losses before charge separation on the J-V curves is similar to the influence of trap-assisted recombination at a low carrier density, which is the dominant factor of the diffusion equation, we account for these losses in the monomolecular recombination term for simplicity. From Equations (6) to (11), the following equation can be obtained:

$$n\mu E = Gd - \left(\frac{1}{\tau} + \gamma n\right)nd, \tag{12}$$

The solution of above equation is:

$$n = \frac{-\left(\mu E + \frac{d}{\tau}\right) + \sqrt{\left(\mu E + \frac{d}{\tau}\right)^2 + 4\gamma Gd^2}}{2\gamma d}, \tag{13}$$

From Equations (6) and (13), the photocurrent can be calculated.

The generation rate, G, was obtained by the transfer matrix method, and other parameters can be extracted from the results of curve fitting, which are listed in Table 5. With these parameters and Equations (9)-(11), one can acquire the amount of the monomolecular recombination and the bimolecular recombination at different applied voltages, as shown in Figure 10. The dominant recombination mechanism in DBP:C_{60} (3:1) is found to be the monomolecular recombination, while the dominant recombination in DBP:C_{60} (1:1) and DBP:C_{60} (1:2) devices is bimolecular recombination. This trend agrees with the surface morphology

observed in the AFM images. DBP:C_{60} (3:1) possess isolated acceptor domains and a small D/A interfacial area, which results in poor exciton dissociation efficiency and simultaneously reduces the possibility for free electrons and holes to encounter each other, resulting in the dominant recombination mechanism being monomolecular recombination. In contrast, DBP:C_{60} (1:1) and DBP:C_{60} (1:2), with interpenetrated domains and a large D/A interfacial area, are dominated by bimolecular recombination.
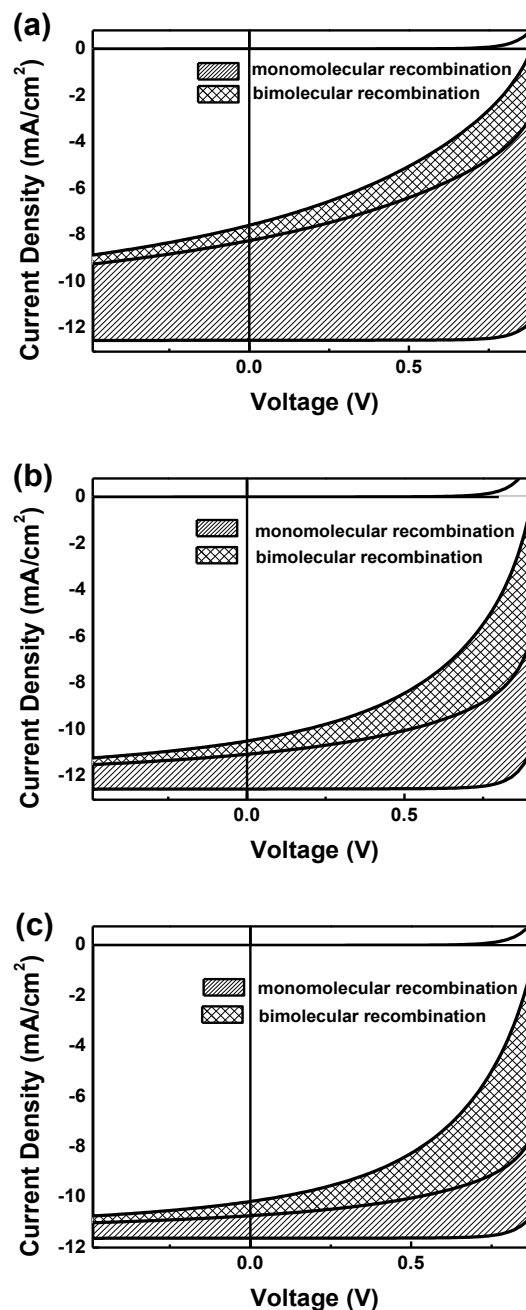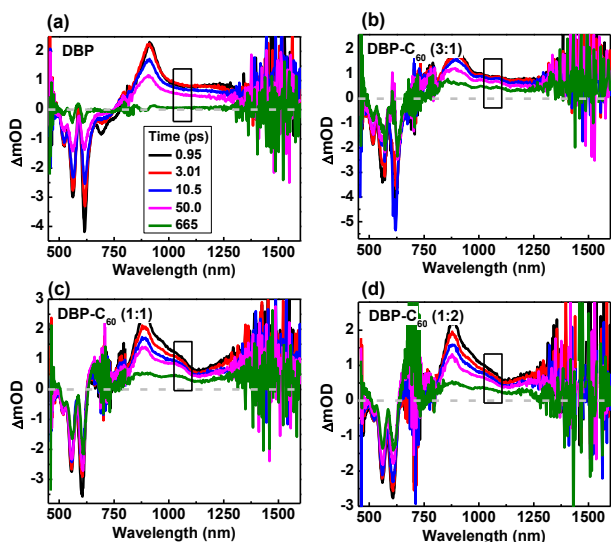

Figure 10. Amount of the monomolecular recombination and the bimolecular recombination at different applied voltages for (a) DBP:C60 (3:1), (b) DBP:C60 (1:1) and (c) DBP:C60 (1:2) PMHJ device.

**Table 5.** The parameters of illumination-intensity dependent J-V curve fitting.

DBP:C_{60}	τ (s)	γ	μ ($cm^2 V^{-1} s^{-1}$)	V_s (V)
3:1	1.4332E-6	1.4018E-11	3.2961E-5	0.9363
1:1	2.4094E-6	3.5432E-11	7.5910E-5	0.9616
1:2	3.2272E-6	5.4347E-11	9.5882E-5	0.9211

Femtosecond transient absorption spectroscopic measurement

fsTA spectra for neat DBP and DBP:C_{60} (3:1, 1:1 and 1:2) films are presented in Figure 11 for the indicated time delays. For neat DBP (Fig. 11(a)), in the visible range, we observe three narrow bleaches (negative photoinduced absorptions (PA)) located at 520, 560 and 616 nm. These bleaches occur at nearly the same wavelengths as the three corresponding peaks in the absorption spectrum of DBP, which suggests a state-filling origin. In the near-infrared, neat DBP exhibits a broad PA with a peak at 910 nm. Introduction of C_{60} produces a clear change in the TA spectra. For all three ratios of DBP:C_{60} investigated (3:1, 1:1 and 1:2, Figures 11(b), (c) and (d), respectively), we observed a peak centred near ~ 890 nm with a shoulder that extends to ~ 1130 nm. This additional structure suggests the formation of a new electronic species. Based upon the spectroelectrochemistry literature, which indicates that C_{60}^{-} yields PA at ~ 1065 nm,[78] we assign the new feature to the formation of C_{60}^{-}. Inspection of the fsTA spectra indicate that DBP:C_{60} mixtures exhibit longer lived spectral features for both the visible and near-IR wavelength ranges.

Figure 11. fsTA dynamics of DBP and DBP:C60 (3:1, 1:1 and 1:2) at 1065 nm over the time range from 0 to 3 ns.

We next investigated the dynamics at 1065 nm for both neat DBP and DBP:C_{60} mixtures (shown in Figure 12). While we could not distinguish distinct rise times at 1065 nm for the mixtures in comparison to neat DBP at early (few picosecond) pump-probe delay times, dissimilar dynamics become apparent at longer times. Specifically, neat DBP decays to negligible signal before 1 ns with a fitted single exponential decay time of 92.2 ± 6.7 ps. The mixtures,
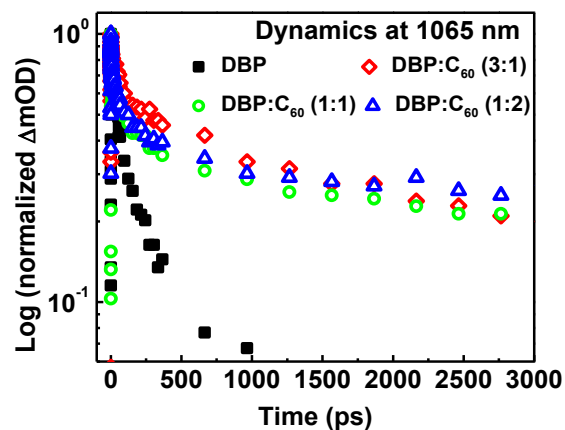
Figure 12. Amount of the monomolecular recombination and the bimolecular recombination at different applied voltages for (a) DBP:C60 (3:1), (b) DBP:C60 (1:1) and (c) DBP:C60 (1:2) PMHJ device.

however, exhibit much longer-lived PA at 1065 nm, which again suggests the formation of C_{60}^{-}. For the respective mixtures of 3:1, 1:1 and 1:2 DBP:C_{60}, the data were fit to biexponential decays with time constants in ps of: 125 ± 26 (36%) and 3055 ± 350 (64%); 27 ± 16 (44%) and 4575 ± 568 (56%); and 92 ± 9 (38%) and 5866 ± 660 (62%). We suggest that the close similarities in the faster decay time constant for each mixture reflects the decay of the DBP that fails to charge separate. The longer decay constant values likely correspond to monomolecular (geminate) electron-hole pair recombination timescales. The DBP:C_{60} (1:2) mixture exhibits the longest lifetime (~ 5.9 ns) of these three mixtures, which suggests that it experiences the lowest amount of monomolecular recombination. These results are consistent with the above-mentioned recombination model, which describes the distribution of monomolecular and bimolecular recombination in a DBP:C_{60} mixture (shown in Figure 10). The recombination of the DBP:C_{60} (3:1) mixture exhibited the lowest amount of bimolecular recombination, while the DBP:C_{60} (1:2) mixture is dominated by bimolecular recombination and exhibited the lowest amount of monomolecular recombination. Here, the fsTA measurements not only revealed the monomolecular recombination dynamics but also further confirmed the accuracy of the recombination model.

Grazing incidence wide-angle X-ray scattering

Grazing incidence wide-angle X-ray scattering (GIWAXS) technology has been applied to extract information about the nano-scale molecular arrangement in thin films, such as crystallite sizes, molecular orientation and intermolecular distances.[8, 79-84] Here, we used GIWAXS to characterize the molecular order and orientation in DBP:C_{60} thin-films. First, we examined the DBP neat film on a Si substrate, and the resulting two-dimensional GIWAXS pattern is shown in Figure 13(a). Compared to the scattering pattern of the reference bare Si (shown in Figure 13(b)), the DBP neat film shows evidence of self-organization within the film. The out-of-plane scattering peak from the (010) Bragg diffraction at $q_z = 1.37$ Å^{-1} is associated with a π-π stacking spacing of 4.58 Å. This result indicates that the π-π stacking of DBP molecules was perpendicular
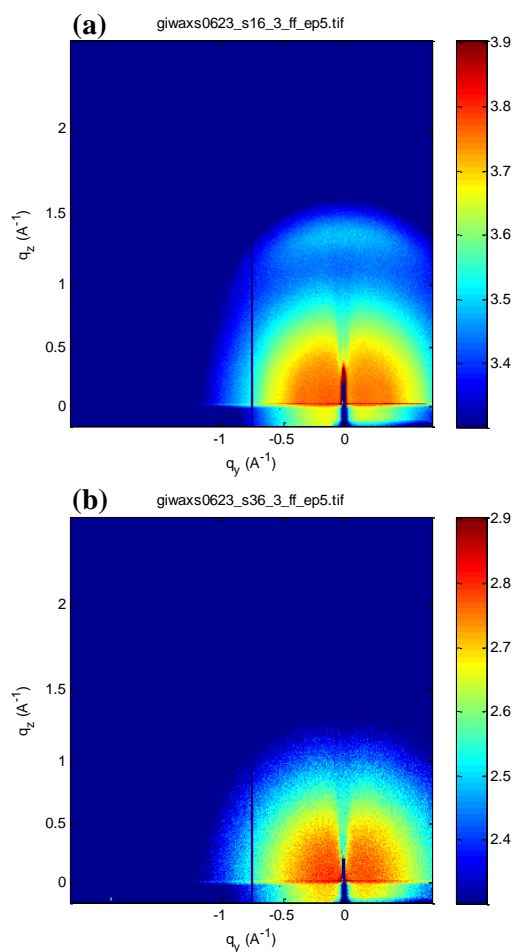
Figure 13. The 2D GIWAXS pattern of (a) DBP neat film on bare Si and (b) bare Si as the control sample.

to the substrate and that the DBP molecules are face-on oriented, which agrees with the anisotropic optical constants and molecular orientation of DBP measured by ellipsometry. Furthermore, we investigated the molecular ordering of the DBP:C_{60} mixtures, which were processed under the same evaporation condition of the devices. Figure 14 shows the 2D GIWAXS pattern of a DBP:C_{60} blend on Si substrates. With C_{60} present, the out-of-plane scattering peak was observed at $q_z = 1.39$ Å^{-1} (d-spacing 4.52 Å), which indicates that DBP molecules are still face-on oriented in DBP:C_{60} thin films and that the stacking spacing of the DBP molecules slightly decreases. In addition, the crystallite size of the DBP lamellae were found to be 6-7 nm for all blend ratios, indicating that the crystallinity of DBP is not affected by the DBP:C_{60} ratio. Two in-plane peaks are observed at $q_y = 0.684$ and 1.325 Å^{-1} for DBP:C_{60} (3:1), 0.690 and 1.335 Å^{-1} for DBP:C_{60} (1:1) and 0.716 and 1.342 Å^{-1} for DBP:C_{60} (1:2), which correspond to the (100) Bragg diffraction, indicating that the C_{60} molecular spacing decreased with the increase of the blend ratio. The different C_{60} stacking spacing may be due to interference from the DBP molecules. As for the out-of-plane peaks from C_{60}, the features at 0.75 Å^{-1} are stronger in-plane than out-of-plane, suggesting that face-on oriented DBP molecules interfere with the C_{60} out-of-plane stacking. The feature of C_{60} at $q_z = 1.34$ Å^{-1} and the feature of DBP are overlapped and thus are difficult to analyze. The

GIWAXS results indicate that the increase of the C_{60} ratio in the blend does not only enhance the interconnection between C_{60} domains but also shorted the average distance of C_{60} molecules, which are both beneficial to electron transport. To eliminate the effect of the substrate on the samples, we further examined the scattering pattern of DBP:C_{60} thin films on Si/PEDOT:PSS (40 nm)/MoO$_3$ (5 nm)/DBP (10 nm) under-layers (as shown in Figure S4). The suppressed scattering peak indicates that the blend thin
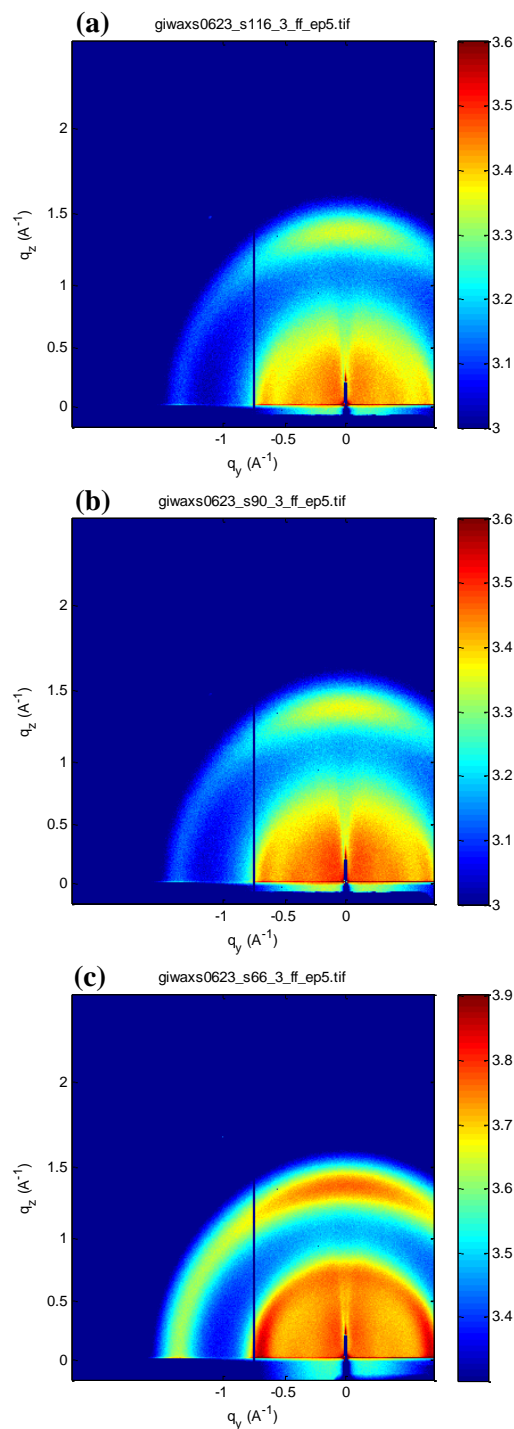

Figure 14. The 2D GIWAXS pattern of (a) DBP:C60 (3:1), (b) DBP:C60 (1:1) and (c) DBP:C60 (1:2) on bare Si.

films in real devices exhibit weaker crystallinity compared to the films on the crystalline silicon substrate. However, except for the different scattering intensities, the same trends were observed in all of the samples regardless of the different under-layers.

Conclusion

In summary, the "all carbon" photovoltaic devices based on the homocyclic molecule DBP as a donor and C_{60} as an acceptor have been comprehensively characterized. The optimized device with a DBP:C_{60} mixture thickness of 20 nm and the ratio of DBP:C_{60} (1:2) exhibited a PCE of 4.47%. Our systematic study revealed some promising advantages of the DBP donor and DBP:C_{60} (1:2) blends for photovoltaic devices. First, the DBP molecules exhibit horizontal orientation, both in DBP neat films and in DBP:C_{60} blends. The face-on stacking could enhance both the absorption of light and the charge carrier mobility. fsTA studies strongly suggest efficient charge separation in the DBP:C_{60} mixtures, with the spectroscopic observation of a long-lived radical anion of C_{60}. Subsequently, DBP:C_{60} (1:2) thin films exhibited not only optimized domain sizes but also partially interconnected acceptor grains, causing a high D/A interfacial area and continuous pathways for electron transport. With the bicontinuous charge carriers pathways, the most balanced carrier mobility and the lowest bi-molecular recombination were found in the DBP:C_{60} (1:2) devices, which exhibited the highest J_{sc}, FF and PCE of the blends studied.

The molecular ordering and crystallinity in DBP neat films and DBP:C_{60} blends were also investigated. The 2D-GIWAXS patterns indicated a face-on stacking of the DBP molecules, both in DBP neat films and in DBP:C_{60} mixtures, which supports the results found in the ellipsometry measurement. In addition, the DBP molecules were found to stack closely, with a π-π stacking spacing of 4.58 Å, indicating an effective molecular orbital overlap in DBP. The close molecular packing of DBP leads to efficient hole transport in the DBP:C_{60} mixture and thus to balanced hole and electron mobilities, especially in the DBP:C_{60} (1:2) thin film. The study not only reveals the promising characteristics of DBP as donors in OSCs but the clear correlations of the thin-film nano-morphology, molecular stacking, carrier mobility and charge recombination found here could also provide insights into the characterization methodology and optimization for the small molecule OSCs.

Experimental

Device fabrication

The donor material, DBP was purchased from *Luminescence Technology Corporation*, and the acceptor material, C_{60}, was purchased from *Nichem Fine Technology Corporation.* All organic materials were purified by temperature-gradient sublimation in a vacuum chamber at a pressure of ~ 1×10^{-6} Torr before usage. The metal oxide, the organic layer and the metal electrodes were thermally deposited in sequence on pre-cleaned indium tin oxide (ITO) glass substrates in an ultra-high vacuum chamber at a base pressure of ~ 1×10^{-6} Torr. The deposition rate of all organic compounds was controlled to a value between 0.3-0.6 Å s^{-1}. The Ag electrode deposition rate was ~ 3 Å s^{-1}. The active area of the

cells had an average size of 5 mm^2, defined by the intersection area between the Ag cathode and the ITO anode. The devices were encapsulated using a UV-cured sealant (*Everwide Chemical Co., Epowide EX*) and a cover glass under an anhydrous nitrogen atmosphere after fabrication and were measured in ambient conditions.

Characteristics measurements

The current density to voltage (*J-V*) characteristics were measured with a *SourceMeter Keithley 2636A* under AM 1.5 G simulated solar illumination at intensity of 100 mW cm^{-2} (calibrated using a NREL-traceable KG5 filtered silicon reference cell). The EQE spectra were obtained by illuminating chopped monochromatic light with a continuous-wave bias white light (from halogen lamp) onto the solar cells. The photocurrent signals were extracted using the lock-in technique with a current preamplifier (*Stanford Research System*) followed by a lock-in amplifier (*AMETEK*). The EQE measurement was fully computer controlled, and the intensity of the monochromatic light was carefully calibrated using an NIST-traceable optical power meter (*Ophir Optronics*). Atomic force microscopy (AFM) images were taken using a Veeco Nanoscope 3100 atomic force microscope. The AC impedance spectroscopy measurement was implemented using a *Reference 600* (*GAMRY Instrument*) potentiostat; the frequency was swept over the range of 10 Hz to 1 MHz. The obtained data were fitted using *EIS300 Electrochemical Impedance Spectroscopy Software* (*GAMRY Instrument*) in terms of the appropriate equivalent circuits. Ellipsometric measurements of the DBP:fullerene thin films over a wavelength range of 300 nm to 1100 nm in steps of 5 nm were performed in air using *J. A. Woollam V-VASE* equipment. The angles of light incidence were varied between 55° and 75° relative to the surface normal in steps of 10° for reflection ellipsometry and between 40° to 60° relative to the surface normal in steps of 10° for transmission ellipsometry. The analysis of the ellipsometric data was performed using the software *WVASE32* (*J. A. Woollam Co.*). Transient photovoltage (TPV) and transient photocurrent (TPC) measurements were obtained using a Nd:YAG laser (*Continuum, Minilite I*) pumped dye laser (Rhodamin 6G, the lasing wavelength range is 555-585 nm with a maximum at 566 nm, pulse width ~ 5 ns) as an excitation source. A 100 W variable intensity halogen lamp was used as the bias light. The transient signals were amplified by a voltage preamplifier (*Stanford Research Systems, SR560*) and a current preamplifier (*Stanford Research Systems, SR570*) for the TPV and TPC measurements, respectively, and were recorded by an oscilloscope (*Tektronix*). Averages of 256 to 512 traces were obtained to improve the signal-to-noise ratio. Femtosecond transient absorption (fsTA) measurements were produced using a 35 fs pulse width, 2 kHz commercial amplified Ti:sapphire laser system operating at 580 nm. Tunable pump pulses were generated with a white-light seeded optical parametric amplifier. A portion (5%) of the amplifier output was mechanically time-delayed and then focused into a 2 mm thick sapphire plate to

produce a white light probe. The pump fluence was 18 µJ cm^{-2} for the fsTA measurements reported below. Films were constantly translated in a raster pattern to prevent the effects of any long-lived charging. No film degradation was observed in the measurements. Grazing Incidence Wide Angle X-ray Scattering (GIWAXS) measurements were performed at Beamline 8-ID-E[85] of the Advanced Photon Source at Argonne National Laboratory. Slits of size of 200 µm (horizontal) and 20 µm (vertical) defined the unfocused beam from the undulator source with a photon energy of 7.35 keV (λ = 1.6868 Å) incident onto the sample at an angle $\alpha_i \approx 0.2°$. The samples were kept under ambient conditions with the Pilatus 1 M pixel array detector (Dectris) positioned 204 mm away. A translation stage allowed the detector to be displaced vertically to compensate for the rows of inactive pixels (172 µm by 172 µm) at the borders between modules. The two-dimensional data, with 20-bit resolution, were stored in 32-bit tif files. The files were corrected for detector non-uniformity, detector sensitivity and solid angle, combined into composite images while eliminating the horizontal rows of the inactive pixels, converted to q-space and integrated into linecuts using the GIXSGUI package for *Matlab* (*The MathWorks, Inc.*). Carrier dynamic modelling program was coded using *Matlab* software (*The MathWorks, Inc.*) and performed using a dual-core *Intel*-CPU desktop computer.

Acknowledgements

Notes and references

^{a}Department of Materials Science and Engineering, National Tsing Hua University, No. 101, Section 2, Kuang-Fu Road, Hsinchu, Taiwan 30013. E-mail: hwlin@mx.nthu.edu.tw
^{b}X-Ray Science Division, Argonne National Laboratory, Argonne, Illinois 60439, United States
^{c}Department of Chemistry, Northwestern University, Evanston Illinois 60208, United States
^{d}Center for Nanoscale Materials, Argonne National Laboratory, Argonne, Illinois 60439, United States
^{e}Research Center for Applied Sciences, Academia Sinica, Taipei 11529, Taiwan

† Electronic Supplementary Information (ESI) available: **1)** Temperature dependent carrier mobility against applied electric flied in DBP:C_{60} (1:1) hole-only and electron-only devices, respectively. **2)** Temperature dependent carrier mobility against applied electric flied in DBP:C_{60} (1:2) hole-only and electron-only devices, respectively. **3)** The Nyquist plots obtained from the DBP:C_{60} PMHJ cells operated under AM1.5G 1 sun simulated solar illumination and V_{oc} condition and the fitting curves calculated by the equivalent circuit. **4)** The 2D GIWAXS pattern of DBP:C_{60} (3:1), DBP:C_{60} (1:1) and DBP:C_{60} (1:2) on Si/PEDOT:PSS/MoO3/DBP, respectively. **5)** The parameters of the equivalent circuit for the cells under AM1.5G solar simulated illumination at intensity of 100 mW/cm^2. See DOI: 10.1039/b000000x/

1. C. W. Tang, *Appl. Phys. Lett.*, 1986, **48**, 183-185.
2. G. Yu, J. Gao, J. C. Hummelen, F. Wudl and A. J. Heeger, *Science*, 1995, **270**, 1789-1791.
3. F. C. Krebs, *Sol. Energy Mater. Sol. Cells*, 2009, **93**, 394-412.
4. L. Huo, J. Hou, S. Zhang, H.-Y. Chen and Y. Yang, *Angew. Chem.*, 2010, **122**, 1542-1545.
5. S. Sista, M.-H. Park, Z. Hong, Y. Wu, J. Hou, W. L. Kwan, G. Li and Y. Yang, *Adv. Mater.*, 2010, **22**, 380-383.
6. L. Zhang, B. Walker, F. Liu, N. S. Colella, S. C. B. Mannsfeld, J. J. Watkins, T.-Q. Nguyen and A. L. Briseno, *J. Mater. Chem.*, 2012, **22**, 4266-4268.
7. Z. He, C. Zhong, S. Su, M. Xu, H. Wu and Y. Cao, *Nat. Photon.*, 2012, **6**, 591-595.
8. W. Chen, T. Xu, F. He, W. Wang, C. Wang, J. Strzalka, Y. Liu, J. Wen, D. J. Miller, J. Chen, K. Hong, L. Yu and S. B. Darling, *Nano Lett.*, 2011, **11**, 3707-3713.
9. S. Pelz, J. Zhang, I. Kanelidis, D. Klink, L. Hyzak, V. Wulf, O. J. Schmitz, J.-C. Gasse, R. Frahm, A. Pütz, A. Colsmann, U. Lemmer and E. Holder, *Eur. J. Org. Chem.*, 2013, **2013**, 4761-4769.
10. P. Peumans and S. R. Forrest, *Appl. Phys. Lett.*, 2001, **79**, 126-128.
11. J. Xue, S. Uchida, B. P. Rand and S. R. Forrest, *Applied Physics Letters*, 2004, **85**, 5757.
12. V. Steinmann, N. M. Kronenberg, M. R. Lenze, S. M. Graf, D. Hertel, K. Meerholz, H. Bürckstümmer, E. V. Tulyakova and F. Würthner, *Adv. Energy Mater.*, 2011, **1**, 888-893.
13. J. Xue, B. P. Rand, S. Uchida and S. R. Forrest, *Adv. Mater.*, 2005, **17**, 66-71.
14. Y. Matsuo, Y. Sato, T. Niinomi, I. Soga, H. Tanaka and E. Nakamura, *J. Am. Chem. Soc.*, 2009, **131**, 16048-16050.
15. R. Pandey, A. A. Gunawan, K. A. Mkhoyan and R. J. Holmes, *Adv. Funct. Mater.*, 2012, **22**, 617-624.
16. M. Riede, C. Uhrich, J. Widmer, R. Timmreck, D. Wynands, G. Schwartz, W.-M. Gnehr, D. Hildebrandt, A. Weiss, J. Hwang, S. Sundarraj, P. Erk, M. Pfeiffer and K. Leo, *Advanced Functional Materials*, 2011, **21**, 3019-3028.
17. D. Wynands, M. Levichkova, K. Leo, C. Uhrich, G. Schwartz, D. Hildebrandt, M. Pfeiffer and M. Riede, *Appl. Phys. Lett.*, 2010, **97**, 073503-073503.
18. G. Chen, H. Sasabe, Z. Wang, X.-F. Wang, Z. Hong, Y. Yang and J. Kido, *Adv. Mater.*, 2012, **24**, 2768-2773.
19. L.-Y. Lin, C.-W. Lu, W.-C. Huang, Y.-H. Chen, H.-W. Lin and K.-T. Wong, *Org. Lett.*, 2011, **13**, 4962-4965.
20. S. Steinberger, A. Mishra, E. Reinold, J. Levichkov, C. Uhrich, M. Pfeiffer and P. Bauerle, *Chem. Commun.*, 2011, **47**, 1982-1984.
21. S. Roquet, A. Cravino, P. Leriche, O. Alévêque, P. Frère and J. Roncali, *J. Am. Chem. Soc.*, 2006, **128**, 3459-3466.
22. H. Kageyama, H. Ohishi, M. Tanaka, Y. Ohmori and Y. Shirota, *Adv. Funct. Mater.*, 2009, **19**, 3948-3955.
23. S. Wang, E. I. Mayo, M. D. Perez, L. Griffe, G. Wei, P. I. Djurovich, S. R. Forrest and M. E. Thompson, *Appl. Phys. Lett.*, 2009, **94**, 233304-233303.

24. R. Fitzner, E. Mena-Osteritz, A. Mishra, G. Schulz, E. Reinold, M. Weil, C. Körner, H. Ziehlke, C. Elschner, K. Leo, M. Riede, M. Pfeiffer, C. Uhrich and P. Bäuerle, *J. Am. Chem. Soc.*, 2012, **134**, 11064-11067.

25. S.-W. Chiu, L.-Y. Lin, H.-W. Lin, Y.-H. Chen, Z.-Y. Huang, Y.-T. Lin, F. Lin, Y.-H. Liu and K.-T. Wong, *Chem. Commun.*, 2012, **48**, 1857-1859.

26. H.-W. Lin, S.-W. Chiu, L.-Y. Lin, Z.-Y. Hung, Y.-H. Chen, F. Lin and K.-T. Wong, *Advanced Materials*, 2012, **24**, 2269-2272.

27. L.-Y. Lin, Y.-H. Chen, Z.-Y. Huang, H.-W. Lin, S.-H. Chou, F. Lin, C.-W. Chen, Y.-H. Liu and K.-T. Wong, *J. Am. Chem. Soc.*, 2011, **133**, 15822-15825.

28. Y.-H. Chen, L.-Y. Lin, C.-W. Lu, F. Lin, Z.-Y. Huang, H.-W. Lin, P.-H. Wang, Y.-H. Liu, K.-T. Wong, J. Wen, D. J. Miller and S. B. Darling, *J. Am. Chem. Soc.*, 2012, **134**, 13616-13623.

29. N. M. Kronenberg, V. Steinmann, H. Bürckstümmer, J. Hwang, D. Hertel, F. Würthner and K. Meerholz, *Adv. Mater.*, 2010, **22**, 4193-4197.

30. S. Yoo, B. Domercq and B. Kippelen, *Appl. Phys. Lett.*, 2004, **85**, 5427-5429.

31. A. K. Pandey and J.-M. Nunzi, *Appl. Phys. Lett.*, 2006, **89**, 213506-213503.

32. S. Yoo, W. J. Potscavage Jr, B. Domercq, S.-H. Han, T.-D. Li, S. C. Jones, R. Szoszkiewicz, D. Levi, E. Riedo, S. R. Marder and B. Kippelen, *Solid State Electron*, 2007, **51**, 1367-1375.

33. D. Cheyns, H. Gommans, M. Odijk, J. Poortmans and P. Heremans, *Sol. Energy Mater. Sol. Cells*, 2007, **91**, 399-404.

34. D. Yokoyama, Z. Qiang Wang, Y.-J. Pu, K. Kobayashi, J. Kido and Z. Hong, *Sol. Energy Mater. Sol. Cells*, 2012, **98**, 472-475.

35. D. Fujishima, H. Kanno, T. Kinoshita, E. Maruyama, M. Tanaka, M. Shirakawa and K. Shibata, *Sol. Energy Mater. Sol. Cells*, 2009, **93**, 1029-1032.

36. M. C. Barr, R. M. Howden, R. R. Lunt, V. Bulović and K. K. Gleason, *Adv. Energy Mater.*, 2012, **2**, 1404-1409.

37. Z. Wang, D. Yokoyama, X.-F. Wang, Z. Hong, Y. Yang and J. Kido, *Energy Environ. Sci.*, 2013, **6**, 249-255.

38. M. Hirade and C. Adachi, *Appl. Phys. Lett.*, 2011, **99**, 153302-153303.

39. M. Hirade, H. Nakanotani, M. Yahiro and C. Adachi, *Acs Appl Mater Inter*, 2010, **3**, 80-83.

40. D. Yokoyama, A. Sakaguchi, M. Suzuki and C. Adachi, *Appl. Phys. Lett.*, 2008, **93**, 173302-173303.

41. H.-W. Lin, C.-L. Lin, C.-C. Wu, T.-C. Chao and K.-T. Wong, *Org. Electron.*, 2007, **8**, 189-197.

42. H.-W. Lin, C.-L. Lin, H.-H. Chang, Y.-T. Lin, C.-C. Wu, Y.-M. Chen, R.-T. Chen, Y.-Y. Chien and K.-T. Wong, *J. Appl. Phys.*, 2004, **95**, 881-886.

43. H.-Y. Lin, W.-C. Huang, Y.-C. Chen, H.-H. Chou, C.-Y. Hsu, J. T. Lin and H.-W. Lin, *Chem. Commun.*, 2012, **48**, 8913-8915.

44. H. Shang, H. Fan, Y. Liu, W. Hu, Y. Li and X. Zhan, *Adv. Mater.*, 2011, **23**, 1554-1557.

45. G. Wei, S. Wang, K. Renshaw, M. E. Thompson and S. R. Forrest, *ACS Nano*, 2010, **4**, 1927-1934.

46. G. Wei, S. Wang, K. Sun, M. E. Thompson and S. R. Forrest, *Adv. Energy Mater.*, 2011, **1**, 184-187.

47. Y. Sun, G. C. Welch, W. L. Leong, C. J. Takacs, G. C. Bazan and A. J. Heeger, *Nat. Mater.*, 2012, **11**, 44-48.

48. W. Brütting, S. Berleb and A. G. Mückl, *Synth. Met.*, 2001, **122**, 99-104.

49. T.-Y. Chu and O.-K. Song, *Appl. Phys. Lett.*, 2007, **90**, 203512-203513.

50. H. Bässler, *Phys. Status Solidi B*, 1993, **175**, 15-56.

51. S. V. Novikov, D. H. Dunlap, V. M. Kenkre, P. E. Parris and A. V. Vannikov, *Phys. Rev. Lett.*, 1998, **81**, 4472-4475.

52. D. Hertel, H. Bassler, U. Scherf and H. H. Horhold, *J. Chem. Phys.*, 1999, **110**, 9214-9222.

53. H. H. Fong, K. C. Lun and S. K. So, *Chem. Phys. Lett.*, 2002, **353**, 407-413.

54. J. You, C.-C. Chen, L. Dou, S. Murase, H.-S. Duan, S. A. Hawks, T. Xu, H. J. Son, L. Yu, G. Li and Y. Yang, *Adv. Mater.*, 2012, **24**, 5267-5272.

55. T. Kuwabara, C. Iwata, T. Yamaguchi and K. Takahashi, *Acs Appl Mater Inter*, 2010, **2**, 2254-2260.

56. S. Ishihara, H. Hase, T. Okachi and H. Naito, *J. Appl. Phys.*, 2011, **110**, 036104-036103.

57. Q. Wang, J.-E. Moser and M. Grätzel, *J. Phys. Chem. B*, 2005, **109**, 14945-14953.

58. L. Han, N. Koide, Y. Chiba and T. Mitate, *Appl. Phys. Lett.*, 2004, **84**, 2433-2435.

59. J. Bisquert, M. Grätzel, Q. Wang and F. Fabregat-Santiago, *J. Phys. Chem. B*, 2006, **110**, 11284-11290.

60. C.-C. Hsiao, A.-E. Hsiao and S.-A. Chen, *Adv. Mater.*, 2008, **20**, 1982-1988.

61. A. Pitarch, G. Garcia-Belmonte, J. Bisquert and H. J. Bolink, *J. Appl. Phys.*, 2006, **100**, 084502-084505.

62. S. Ishihara, H. Hase, T. Okachi and H. Naito, *Org. Electron.*, 2011, **12**, 1364-1369.

63. F. Fabregat-Santiago, G. Garcia-Belmonte, I. Mora-Sero and J. Bisquert, *PCCP*, 2011, **13**, 9083-9118.

64. P. P. Boix, A. Guerrero, L. F. Marchesi, G. Garcia-Belmonte and J. Bisquert, *Adv. Energy Mater.*, 2011, **1**, 1073-1078.

65. B. J. Leever, C. A. Bailey, T. J. Marks, M. C. Hersam and M. F. Durstock, *Adv. Energy Mater.*, 2012, **2**, 120-128.

66. H.-W. Lin, C.-W. Lu, L.-Y. Lin, Y.-H. Chen, W.-C. Lin, K.-T. Wong and F. Lin, *J. Mater. Chem. A*, 2013, **1**, 1770-1777.

67. M. Glatthaar, M. Riede, N. Keegan, K. Sylvester-Hvid, B. Zimmermann, M. Niggemann, A. Hinsch and A. Gombert, *Sol. Energy Mater. Sol. Cells*, 2007, **91**, 390-393.

68. C. G. Shuttle, B. O'Regan, A. M. Ballantyne, J. Nelson, D. D. C. Bradley, J. de Mello and J. R. Durrant, *Appl. Phys. Lett.*, 2008, **92**, 093311-093313.

69. R. Hamilton, C. G. Shuttle, B. O'Regan, T. C. Hammant, J. Nelson and J. R. Durrant, *J. Phys. Chem. Lett.*, 2010, **1**, 1432-1436.

70. M. Hirade, T. Yasuda and C. Adachi, *J. Phys. Chem. C*, 2013, **117**, 4986-4991.

71. D. Credgington, R. Hamilton, P. Atienzar, J. Nelson and J. R. Durrant, *Adv. Funct. Mater.*, 2011, **21**, 2744-2753.

72. Y.-S. Kim, T. Kim, B. Kim, D.-K. Lee, H. Kim, B.-K. Ju and K. Kim, *Org. Electron.*, 2013, **14**, 1749-1754.

73. L. J. A. Koster, V. D. Mihailetchi and P. W. M. Blom, *Appl. Phys. Lett.*, 2006, **88**, 052104-052103.

74. M. M. Mandoc, L. J. A. Koster and P. W. M. Blom, *Appl. Phys. Lett.*, 2007, **90**, 133504-133503.

75. R. A. Street, M. Schoendorf, A. Roy and J. H. Lee, *Phys. Rev. B*, 2010, **81**, 205307.

76. T. M. Clarke and J. R. Durrant, *Chem. Rev.*, 2010, **110**, 6736-6767.

77. S. Shoaee, M. P. Eng, E. Espildora, J. L. Delgado, B. Campo, N. Martin, D. Vanderzande and J. R. Durrant, *Energy Environ. Sci.*, 2010, **3**, 971-976.

78. D. R. Lawson, D. L. Feldheim, C. A. Foss, P. K. Dorhout, C. M. Elliott, C. R. Martin and B. Parkinson, *J. Electrochem. Soc.*, 1992, **139**, L68-L71.

79. W. Chen, M. P. Nikiforov and S. B. Darling, *Energy Environ. Sci.*, 2012, **5**, 8045-8074.

80. W.-R. Wu, U. S. Jeng, C.-J. Su, K.-H. Wei, M.-S. Su, M.-Y. Chiu, C.-Y. Chen, W.-B. Su, C.-H. Su and A.-C. Su, *ACS Nano*, 2011, **5**, 6233-6243.

81. H.-C. Liao, C.-S. Tsao, T.-H. Lin, C.-M. Chuang, C.-Y. Chen, U. S. Jeng, C.-H. Su, Y.-F. Chen and W.-F. Su, *J. Am. Chem. Soc.*, 2011, **133**, 13064-13073.

82. H. Sirringhaus, P. J. Brown, R. H. Friend, M. M. Nielsen, K. Bechgaard, B. M. W. Langeveld-Voss, A. J. H. Spiering, R. A. J. Janssen, E. W. Meijer, P. Herwig and D. M. de Leeuw, *Nature*, 1999, **401**, 685-688.

83. M.-S. Su, C.-Y. Kuo, M.-C. Yuan, U. S. Jeng, C.-J. Su and K.-H. Wei, *Adv. Mater.*, 2011, **23**, 3315-3319.

84. N. D. Eisenmenger, G. M. Su, G. C. Welch, C. J. Takacs, G. C. Bazan, E. J. Kramer and M. L. Chabinyc, *Chem. Mater.*, 2013, **25**, 1688-1698.

85. Z. Jiang, X. Li, J. Strzalka, M. Sprung, T. Sun, A. R. Sandy, S. Narayanan, D. R. Lee and J. Wang, *Journal of Synchrotron Radiation*, 2012, **19**, 627-636.